The effect of low Cu additions on precipitate crystal structures in overaged Al-Mg-Si(-Cu) alloys

Jonas K. Sunde[a],*, Calin D. Marioara[b], Randi Holmestad[a]

[a] *Department of Physics, Norwegian University of Science and Technology (NTNU), Trondheim N-7491, Norway*
[b] *Materials and Nanotechnology, SINTEF Industry, Trondheim N-7465, Norway*
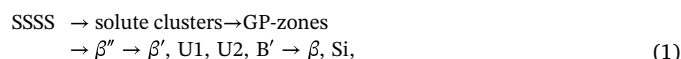
ABSTRACT

This study concerns the effect of low Cu additions ($\lesssim$0.1 at.%) on the precipitate crystal structure evolution in three Al-Mg-Si(-Cu) alloys during overageing. The evolution was assessed through a combination of atomic resolution scanning transmission electron microscopy, scanning electron diffraction, and differential scanning calorimetry. It was found that relatively small changes in the Cu level and the Si:Mg ratio had significant effects on the resulting distribution of precipitate phases, their structural evolution, and their thermal stability. Two Si-rich alloys formed hybrid β' phase and Q' phase precipitates on overageing. A third Mg-rich alloy primarily formed L phase precipitates, which exhibited superior thermal stability. Three distinct Cu-containing sub-units that form the basis for all Al-Mg-Si-Cu precipitate phases were identified: the three-fold symmetric Q'/C and the β_{Cu}' sub-units, in addition to a newly discovered C sub-unit. The formation of each sub-unit was discussed, and the atomic structures and connections to other precipitate phases in the Al-Mg-Si(-Cu) system were elaborated. The work presented provides new insights into the complex precipitation of Cu-added Al-Mg-Si alloys, with implications for material properties. The results obtained will be of importance in future alloy and process development, and are thought to be of high value in modelling work on the quaternary Al-Mg-Si-Cu system.

1. Introduction

Heat treatable (age hardenable) 6xxx series Al-Mg-Si(-Cu) alloys form an important group of medium strength engineering alloys widely applied in the transportation and construction sector. This alloy series can be tailored to exhibit a favourable combination of properties, including good formability, high strength-to-weight ratio, and good corrosion resistance [1, 2]. The 6xxx series Al alloys obtain a large increase in hardness when subjected to short-term thermal ageing. The hardening is due to a high number of nano-sized and metastable precipitate phases that form and distribute throughout the Al matrix [3, 4]. The various phases have different atomic structures, and therefore differ in mechanical properties. The phases also vary in atomic matchings at the precipitate-matrix interface, which cause different levels of interfacial strain. Dislocation movement is impeded by both the atomic structure of precipitate phases and the interfacial strain, which results in material strengthening. Consequently, the properties of an alloy depend strongly on the precipitate types and the microstructures they produce.
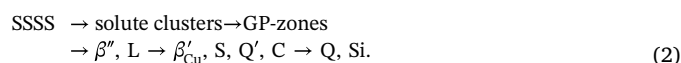
The total addition of precipitate forming elements Mg, Si, and Cu typically amounts to < 2 at.% in wrought 6xxx series Al alloys. Changes in the Cu level and the Si:Mg ratio may have a pronounced effect on the resulting distribution of precipitates (types, sizes, density, etc.). Rod- or lath-shaped precipitates with long axes parallel to $\langle 100 \rangle_{Al}$ are characteristic of the Al-Mg-Si-Cu system. In the Cu-free system, the established precipitation sequence is given as [5, 6]

$$\begin{aligned} \text{SSSS} \quad &\rightarrow \text{solute clusters} \rightarrow \text{GP-zones} \\ &\rightarrow \beta'' \rightarrow \beta', \text{U1, U2, B}' \rightarrow \beta, \text{Si,} \end{aligned} \quad (1)$$

where SSSS denotes a supersaturated solid solution.

There is a large commercial interest in Cu additions in Al-Mg-Si alloys as it is demonstrated to increase the age hardening response, and to promote a higher number density of smaller precipitates that exhibit improved thermal stability [7-12] . The addition of Cu leads to a more complex precipitation sequence, that can be stated as [7, 13-16]

$$\begin{aligned} \text{SSSS} \quad &\rightarrow \text{solute clusters} \rightarrow \text{GP-zones} \\ &\rightarrow \beta'', \text{L} \rightarrow \beta_{Cu}', \text{S, Q}', \text{C} \rightarrow \text{Q, Si.} \end{aligned} \quad (2)$$

All metastable precipitate phases in the Al-Mg-Si(-Cu) system are structurally related due to a common network of Si atomic columns along the precipitate lengths [13]. In $\langle 100 \rangle_{Al}$ projection, this network exhibits a near hexagonal symmetry with $a = b \approx 4$ Å. For the β'' phase, the network is partly fragmented due to a high coherency with

---

* Corresponding author.
  E-mail address: jonas.k.sunde@ntnu.no (J.K. Sunde).

the Al matrix [17]. The different types of precipitates are distinguished based on how their Al, Mg, and Cu atomic columns are positioned with respect to the Si-network columns. Al and Mg are always positioned in-between the Si-network columns, and Cu is positioned in-between (Q' phase and C phase), or replacing parts of the Si-network columns (β_{Cu}' phase) [18]. The precipitate atomic columns can also exhibit variations in atomic modulation and/or mixed element occupancy. In the precipitation sequence Eq. (2), the frequently used notations QP and QC are not included, being instead interpreted as fragments of Al-Mg-Si (-Cu) phases on the Si-network and the β_{Cu}' phase, respectively. The details of this discussion are presented in the reviews conducted by Saito et al. [19] and Andersen et al. [20].

As noted, Cu additions are generally associated with several favourable effects, but are on the other hand also causing an increased susceptibility towards corrosion [21]. Pitting- and intergranular corrosion (IGC), are the two most common corrosion modes observed in this alloy system [22]. IGC mainly occurs when the alloys are artificially aged and when Cu > 0.1 wt.% and/or contain excess Si compared to the β phase stochiometry (Mg$_2$Si) [23]. IGC is thought to propagate due to the presence of a continuous Cu film along grain boundaries (GBs), and an increase in IGC resistance at overaged conditions is thought to be due to the induced discontinuity in this film [24, 25]. If this is the case, then the key towards limiting IGC is therefore to maximize Cu absorption in bulk precipitates, leaving less Cu available to form a continuous Cu film at the GBs [26]. Further research is necessary to improve alloy compositions and thermomechanical processing routines that lead to alloys exhibiting satisfactory corrosion properties, as well as enhanced strength and thermal stability. Therefore, it is important to obtain an improved understanding of how Cu is incorporated into the precipitate structures, which was explored in the present study.

Due to the aforementioned considerations it was decided to focus on low Cu additions ($\lesssim 0.1$ at.%). At these Cu levels, fragmentation and hybridization often prevails, with the different phase unit cells and sub-structures of the Al-Mg-Si- and the Cu-added system often coexisting within individual precipitates [18, 27]. Low level additions are also highly relevant on the subject of Al alloy recycling. There are vast energy savings in re-using Al alloys, and recycling is an important activity in the industry [28]. Recycled Al alloys will inevitably contain certain levels of trace elements, which might induce undesirable changes to the precipitation, as relatively low amounts of solute elements are needed to form precipitates. These changes could have consequences for the mechanical properties of the alloy. The influence of Cu as a trace element on precipitation was another aspect studied through this work.

In the present work, atomic resolution scanning transmission electron microscopy (STEM) was used to assess the precipitate structures, and the distribution of 1000s of precipitate phases was quantified using a recently developed scanning precession electron diffraction (SPED) approach [29, 30]. Electron microscopy results were linked to bulk material phase transformations measured by differential scanning calorimetry (DSC). The combination of techniques provided a detailed assessment of the evolution of phases in the alloy microstructures as a function of overageing, with particular focus on the role of Cu.

2. Experimental procedures

2.1. Materials and heat treatments

Three Al-Mg-Si(-Cu) alloys with different, albeit low Cu additions were studied. Table 1 shows the compositions of the alloys. The compositions of alloys S and C correspond with the high strength commercial alloy 6082, whereas alloy M falls outside of this range. On comparison with alloys S and C, alloy M differs by being Mg-rich, has a higher level of Cu, and lower concentration of the dispersoid (/primary particle) forming elements Mn and Cr. The alloys were delivered as extruded rods (Ø 30 mm). Approximately 10 mm height cylinders were

Table 1
Nominal compositions of the three Al-Mg-Si(-Cu) alloys studied.

Alloy	Al	Si	Mg	Cu	Fe	Mn	Cr
S at.%	Bal.	0.85	0.80	0.01	0.12	0.25	0.08
S wt.%	Bal.	0.88	0.72	0.03	0.24	0.51	0.16
C at.%	Bal.	0.85	0.71	0.04	0.10	0.22	0.07
C wt.%	Bal.	0.88	0.64	0.09	0.20	0.45	0.14
M at.%	Bal.	0.62	0.86	0.10	0.13	0.13	0.01
M wt.%	Bal.	0.64	0.77	0.23	0.26	0.26	0.02

cut from the rods and set to solution heat treatment at 540 °C for 12 min conducted in a salt bath. Subsequently, the specimens were water-quenched to room temperature and kept at this temperature for 10 min before they were artificially aged at 180 °C conducted in an oil bath. The material conditions selected for TEM studies were chosen as follows: alloy S — 3 h, 12 h, 24 h, 1 week, 2 weeks, and 1 month ageing; alloy C — 3 h, 12 h, 24 h, and 1 week ageing; alloy M — 3 h, 24 h, and 1 month ageing.

2.2. Preparation of TEM specimens

The heat treated material cylinders were cut to 1 mm height and then mechanically polished with gradually finer grades of SiC-paper until they reached a thickness of roughly 100 μm. Al discs of 3 mm diameter were punched out from the polished cylinders. Subsequently, the discs were electro-polished using a Struers Tenupol-5 applying an electrolytic solution comprising a 2:1 mixture of methanol:nitric acid, kept between − 30 °C and -25 °C. The voltage was set to 20 V (current 0.2 A). A Fischione 1020 Plasma Cleaner was used on each specimen prior to TEM studies in order to minimize carbon contamination.

2.3. Electron microscopy

Initial visualization of the alloy microstructures was done using bright-field TEM imaging, which was attained using a JEOL 2100 microscope operated at 200 kV. A double corrected JEOL ARM200F microscope (200 kV) was used to obtain atomically resolved high-angle annular dark-field (HAADF) STEM lattice images. The detector collection angle used was 42–178 mrad.

SPED experiments were performed using a JEOL 2100F microscope (200 kV). The microscope is equipped with a NanoMEGAS ASTAR system which makes it possible to simultaneously scan the electron beam while recording electron diffraction patterns. The diffraction patterns that were formed on the phosphor viewing screen of the microscope were captured using an external Allied Vision StingRay camera [31]. The nanobeam diffraction mode was used when running SPED, and the beam alignment for PED was done using the procedure described by Barnard et al. [32]. The following parameters were used when acquiring SPED data: probe diameter — 0.5–2.0 nm (non-precessed); probe semi-convergence angle — 1.0 mrad; precession angle — 0.5, 0.7, or 1.0°; precession frequency — 100 Hz; scan step size — 0.76, 1.52, or 2.28 nm; and exposure time — 20 or 40 ms per pixel. The precipitate distribution (sizes, density, etc.) change with thermal ageing, and the acquisition parameters had to be adjusted to cover representative numbers of precipitates for each alloy and ageing condition.

SPED can be classified as a 4D-STEM technique, and each dataset is composed of 2D PED patterns associated with each pixel in a 2D scan area. The HyperSpy [33] Python library was used for data visualization and analysis. The SPED data formed the basis for estimating average precipitate phase fractions in the microstructure of the different alloys after various ageing times. The details of the SPED data analysis is elaborated in a previously related work by Sunde et al. [30].
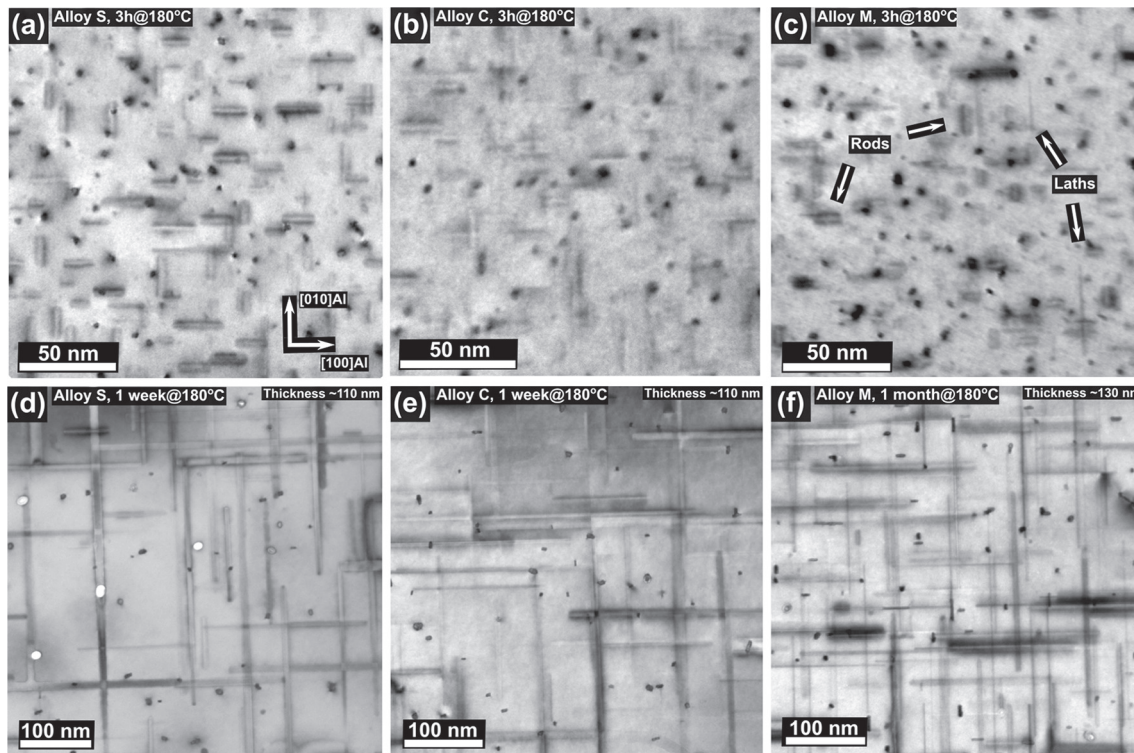
Fig. 1. (a–f) Bright-field TEM images of indicated alloys and ageing times. All images are acquired near the $[001]_{Al}$ zone axis.

Table 2
Average precipitate parameters in alloys S, C, and M for selected ageing conditions.

Alloy & condition	Cross-section area	Length rods	Length laths
S 3 h	(13 ± 1) nm²	(14 ± 1) nm	–
S 1 week	(45 ± 3) nm²	(242 ± 7) nm	–
C 3 h	(10 ± 1) nm²	(13 ± 1) nm	–
C 1 week	(55 ± 3) nm²	(181 ± 6) nm	–
M 3 h	(10 ± 1) nm²	(11 ± 1) nm	(25 ± 2) nm
M 1 month	(43 ± 3) nm²	(136 ± 4) nm*	(136 ± 4) nm*

  * Coarsened precipitates lying in-plane were not clearly separable as rods and laths and were assumed to be approximately equal in size.

2.4. Thermal analysis by DSC

DSC experiments were conducted for alloys S and C, and employed a Hitachi DSC7020 using a heating rate of ~0.2 K s^{-1} (10 K min^{-1}) scanned from RT (~25 °C) up to 500 °C. Specimens were measured relative to a thermodynamically inert reference specimen of pure aluminium with equal geometry, using nitrogen as purge gas. The specimens were cut to cubic geometry (5:5:5 [mm], h:l:w) with masses of (21 ± 1) mg. DSC experiments were conducted on four material conditions: as-solutionized (~10 min natural ageing), 3 h, 24 h, and 1 week ageing at 180 °C. This corresponds to an as-solutionized, peak aged, medium overaged, and significantly overaged condition, respectively. DSC diagrams are presented using excess specific heat capacity, c_p [J g^{-1} K^{-1}], calculated as [34]

$$c_p = \frac{\dot{Q}_S - \dot{Q}_B}{m_S \cdot \epsilon},$$

where $\dot{Q}_S$ and $\dot{Q}_B$ are the specimen and baseline heat flows, respectively. m_S denotes the specimen mass, and ϵ is the heating rate. The baseline heat flow was obtained by scanning a pure Al specimen against

another pure Al reference specimen in the DSC device using identical scan parameters as for the scanned alloy conditions.

3. Results and discussion

3.1. Assessment of the precipitate crystal structure evolution by TEM

The transformations of the alloy microstructures after different ageing times at 180 °C are shown in Fig. 1. At 3 h ageing (peak aged), the microstructures comprised high densities of short rods with characteristic β'' strain fields on either side, running parallel to the main growth direction. In alloy M, longer and narrow lath-shaped precipitates were also visible (highlighted). As will be shown in the following, these precipitates are mainly L phases, and do not exhibit the same strain contrast characteristic of β''. After 1 week ageing, the precipitates in alloys S and C had coarsened considerably as compared to the 3 h condition. The precipitates in alloy M exhibited high resistance towards coarsening, and after 1 month ageing they were still smaller than the precipitates at the 1 week ageing condition in alloys S and C. The average precipitate lengths and the average cross-section areas measured for alloys S, C, and M for the conditions imaged in Fig. 1 are listed in Table 2.

The crystal structures of the main Al-Mg-Si(-Cu) precipitate phases relevant to this work are shown in Fig. 2. HAADF-STEM lattice images of precipitates from corresponding ageing times for alloys S and C are shown in Fig. 3. Fig. 4 shows precipitates from the three studied ageing conditions for alloy M. Fast Fourier transform (FFT) filtering was applied to reduce noise using a circular band pass mask removing all periods shorter than 1.5 Å. Chosen precipitates were evaluated as representative for each ageing condition, but it should be noted that large variations were observed. The same images without highlighting are presented in **Fig. SI 1** and **Fig. SI 2** in the **Supplementary Information (SI)**. **Figs. SI 3–5** present additional HAADF-STEM images of precipitates in all studied alloys and ageing conditions.
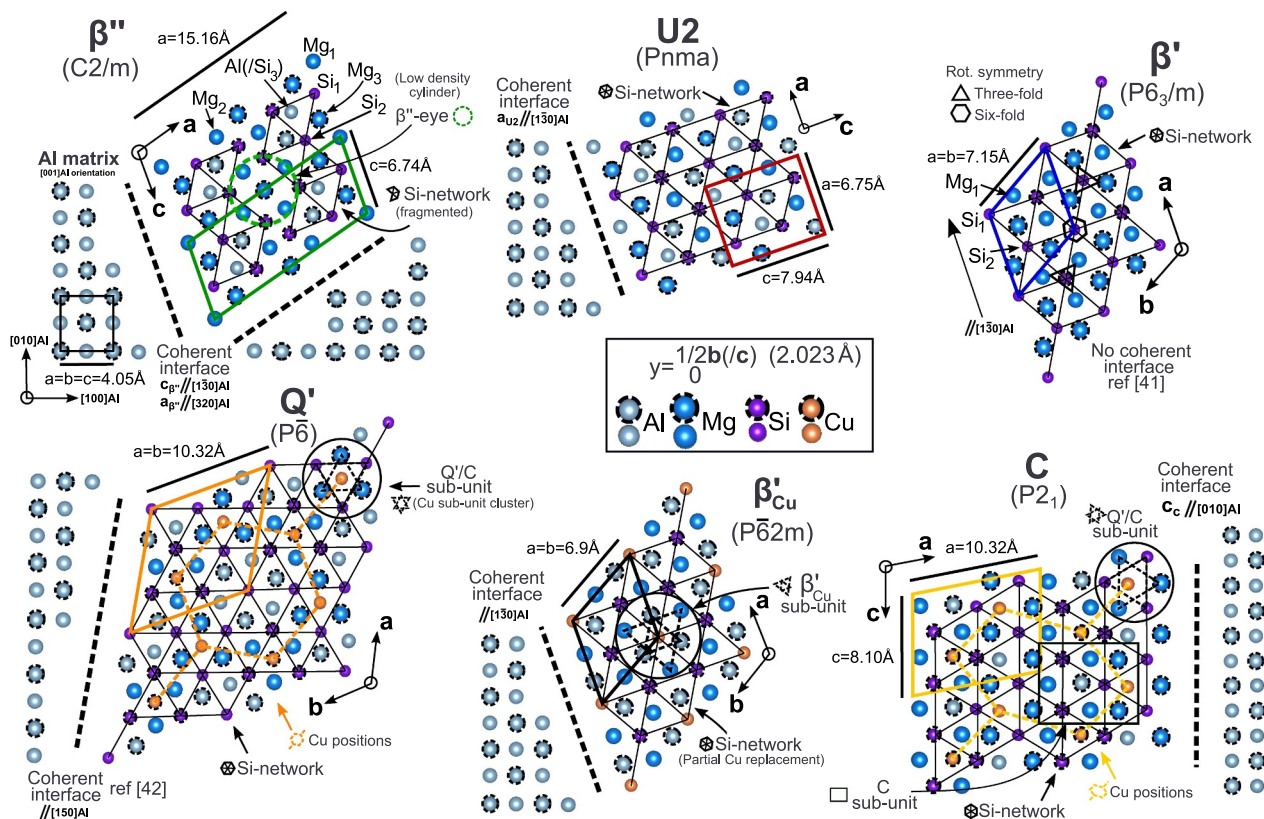
Fig. 2. The crystal structures of the main precipitate phases observed in the present work. Unit cells, sub-units, and other key structural features are indicated. Phase unit cells are shown in coloured full lines. Coherent precipitate-matrix interfaces are indicated for the different phases. The notation $\mathbf{a}_A$, $\mathbf{b}_A$, and $\mathbf{c}_A$ for a given phase A denotes the main crystallographic vectors spanning the unit cell of phase A. The references used for the precipitate crystal structures are shown in **Table SI 1** in the **Supplementary Information (SI)**. (For interpretation of the references to colour in this figure legend, the reader is referred to the web version of this article.)

3.1.1. Peak aged precipitates (3 h ageing)

The vast majority of precipitates in alloys S and C at 3 h ageing was pure β'', see Fig. 3a–d. Some atomic columns in the β'' structures showed higher intensity than the other corresponding columns due to partial occupancy of Cu. Cu ($Z_{Cu} = 29$) exhibits a higher contrast in the HAADF-STEM imaging mode than the other precipitate forming elements Mg ($Z_{Mg} = 12$), Al ($Z_{Al} = 13$), and Si ($Z_{Si} = 14$) due to the $Z^{1.7-2.0}$ atom column scattering power dependency at high angles [35]. The incorporation of Cu in β'' structures was observed to be higher for alloy C than for S, which was as expected due to its higher Cu content. This finding was also supported by the observation of individual β_{Cu}' sub-units in the β'' structures, which were seen in some precipitates in alloy C (e.g. Fig. 3c), but not in alloy S. β_{Cu}' is the Cu-containing equivalent to the isostructural Ag-containing β' phase [36]. The presence of this sub-unit in alloy C was an indication of accelerated phase transformation kinetics occurring for alloy C in comparison to alloy S, which is mainly attributed to the increased Cu content of alloy C.

In the following, the description of precipitate structures uses terms such as phase, sub-unit, hybrid, and fragmented. Here, a precipitate phase means a crystal structure consisting of at least one full unit cell of a phase such as those in the precipitation sequences Eqs. (1) and (2). A sub-unit is used to denote a structural unit that forms part of a precipitate phase unit cell. The term hybrid is used to describe a precipitate that exhibits multiple coexisting phases, all of which form multiple complete phase unit cells. I.e. hybrid precipitates comprise more than one clearly identifiable phase. A fragmented precipitate structure is used to describe a precipitate that comprises multiple phase sub-units or single stray unit cells. Fragmented precipitate structures contain no dominating phase(s). For the latter case, we avoid the term disordered, which is not a clear term in this context. As noted, all precipitate phases in this alloy system build on an underlying Si-network, and comprise

structural units that adhere to this network. Therefore, the precipitates are never truly disordered.

Precipitates in alloy M exhibited notable differences as compared to alloys S and C at 3 h ageing (see Fig. 4a–d). The precipitates can be divided into two types: a fragmented/β'' type (Fig. 4a, b) and an overall fragmented type containing no dominant phase (Fig. 4c, d). The fragmented/β'' type showed significantly increased Cu incorporation as compared to the β'' precipitates in alloys S and C. The β_{Cu}' and the Q'/C sub-units were observed (Fig. 4a), in addition to complete unit cells of Q' and U2 (Fig. 4b). The precipitate shown in image Fig. 4c is classified as L phase. The L phase displays local regions containing unit cells of Q' and C phases (or sub-units), ordered on the Si-network, which aligns with $\langle 100 \rangle_{Al}$. The Si arrangement is the main ordering observed for this phase [37, 38]. Image Fig. 4d shows a precipitate lacking an ordered, permeating Si-network. Furthermore, it does not contain any phase unit cells, and is therefore described as a fragmented precipitate, denoted S phase [16].

There was a tendency of Cu enrichment in certain atomic columns along the precipitate-matrix interface for both types of precipitates in alloy M. Cu segregation to the interface of β'' type precipitates has been observed previously, and was proposed as a mechanism to suppress misfit dislocations [39]. However, here the Cu segregation often takes on a special configuration, highlighted in Fig. 4b, c. In a recent investigation by Weng et al. [40], the same Cu segregation was observed in L type precipitates. It was proposed to arise due to a strong covalent bonding between Cu and Si, where the Si column forms part of the Si-network. As will be shown in the following, this Cu segregation was observed in the majority of all precipitate types in alloy M. On closer inspection, the sub-structure associated with this Cu segregation is seen to be a sub-unit of the C phase, and is therefore denoted as C sub-unit in the following.
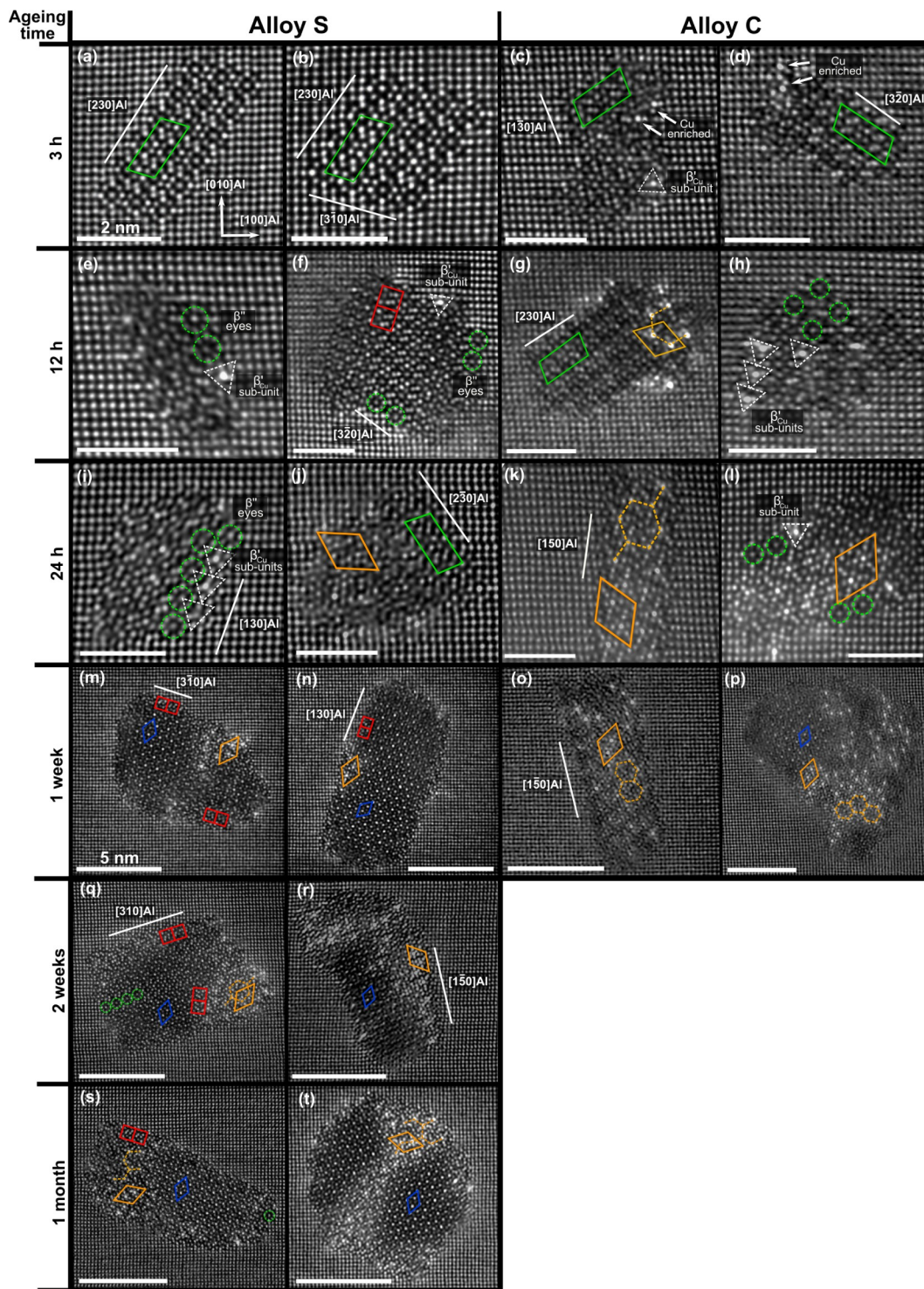
Fig. 3. (a–t) HAADF-STEM lattice images of precipitates from indicated alloys and ageing conditions. A few unit cells, sub-units, and other key structural features of the identified Al-Mg-Si-Cu phases are highlighted, using the marking shown in Fig. 2. Al matrix directions that run parallel to the adjacent precipitate interfaces are indicated. The scale bars (a–l) equal 2 nm, and the scale bars (m–t) correspond to 5 nm.

The observations made for alloy M indicated that the increased Cu content in this alloy as compared to both alloys S and C lead to further enhanced phase transformation kinetics. Some precipitates in alloy M had already formed complete cells of Q′ and C, sub-units of which were not observed in alloys S and C. $\beta_{Cu}′$ sub-units were also more frequent in alloy M as compared to alloy C. In addition to being promoted by increased Cu levels, the fragmentation and formation of L phases were also due to the increased Mg:Si ratio in alloy M as compared to alloys S

and C.

Three distinct Cu-containing sub-units were observed up to this point: the Q′/C sub-unit, the $\beta_{Cu}′$ sub-unit, and a newly discovered C sub-unit. The atomic configuration of these sub-units are shown in Fig. 2. The differences between the three-fold symmetric sub-units of Q′/C and $\beta_{Cu}′$ include the positioning of the Cu column with respect to the Si-network columns. For $\beta_{Cu}′$, the Cu column *replaces* a Si-network column, whereas for Q′/C the column is located *in-between* the network.
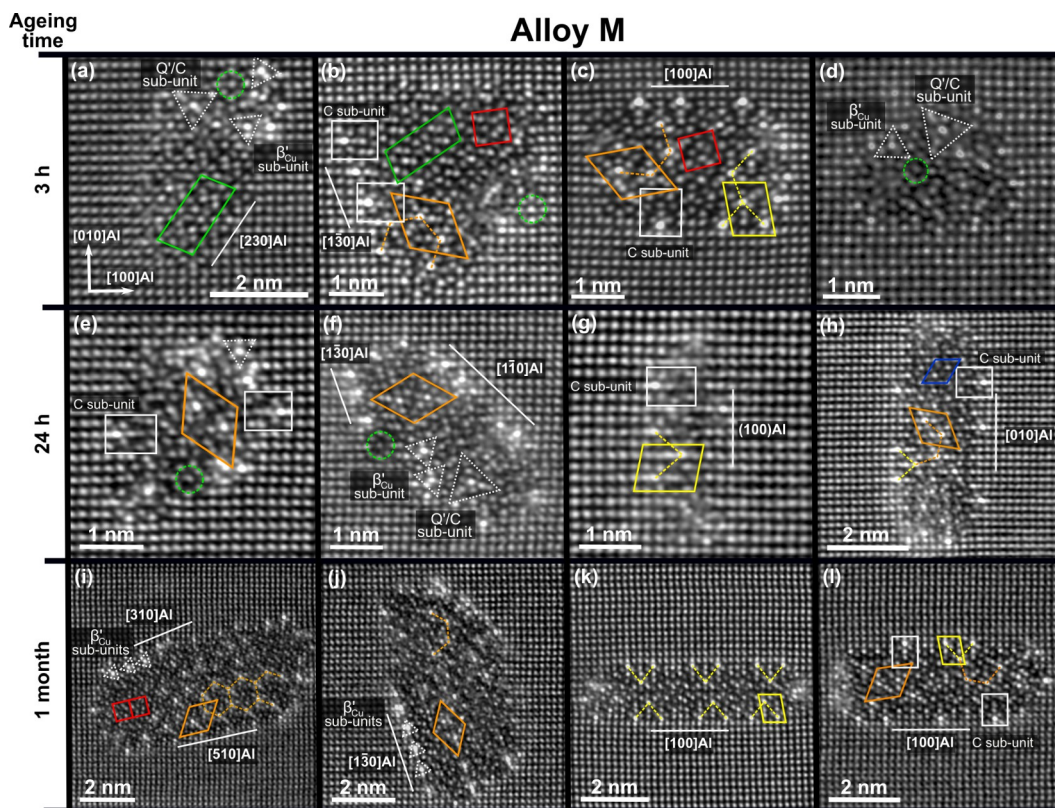
Fig. 4. (a–l) HAADF-STEM lattice images of precipitates from indicated ageing conditions in alloy M. A few unit cells, sub-units, and other key structural features of the identified Al-Mg-Si-Cu phases are highlighted, using the marking shown in Fig. 2. Al matrix directions that run parallel to the adjacent precipitate interfaces are indicated.

Furthermore, the structures differ in the atomic species and interatomic distances of the triangular sites surrounding the center Cu atom. A Mg and a Si triangle is placed at the same atomic height as the Cu atom for the β_{Cu}' and the Q'/C sub-unit, respectively. An Al and a Mg triangle is shifted $c/2 \approx 2.023$ Å in height relative to the center Cu atom for the β_{Cu}' and the Q'/C sub-unit, respectively.

3.1.2. Classification of Al-Mg-Si(-Cu) phases and sub-units

In the literature, there exists other notations for some of the phases and sub-units in the Al-Mg-Si(-Cu) system, some of which are included in Fig. 2. The multiple conventions cause confusion and may lead to misunderstandings. Therefore, for the sake of clarification, **Table SI 1** shows an overview of the present work's labelling together with other existing notations. **Fig. SI 6** shows a flow chart for classifying the different Cu-containing phases.

The Q'/C sub-unit is referred to as a *(Cu) sub-unit cluster* in the work of Cayron et al. [13] and Ding et al. [43], and is proposed as a key building block in the evolution of phases in the Al-Mg-Si-Cu system. In the work of Maeda et al. [44] the same term is used, but then indicating a β_{Cu}' sub-unit. The Q'/C sub-unit is discriminated, and there referred to as a Q' sub-unit cell. Hence, there exists an inconsistency in the terminology used to denote these structural units, which needs to be resolved.

We argue here that it is important to differentiate between the two flavours of Cu-centered, three-fold symmetric sub-units Q'/C and β_{Cu}'. This is because their atomic configurations differ, and hence their formation and subsequent evolution will vary. In addition to the C sub-unit, these in total three sub-units constitute the building blocks for the subsequent formation of all Cu-containing phases in this alloy system. **Fig. SI 7** shows an atomic overlay of a precipitate containing all three sub-units, which serves as a useful illustration of the configuration of the sub-units and how these relate to the Si-network.

3.1.3. Medium overaged precipitates (12 h & 24 h ageing)

At 12 h ageing, unit cells of phases other than β'' were present in alloys S and C (Fig. 3e–h), including U2, β', and Q' (not all shown). This often resulted in a hybrid precipitate structure comprising multiple coexisting phases. Clearer differences between alloys S and C had emerged, the most prominent being the increased proportion of Cu-containing phase unit cells and sub-units in alloy C. In alloy S, unit cells of U2 were often observed to connect to the unit cells of β'', or its sub-units (β''-eyes). The β_{Cu}' sub-unit was also observed for some precipitates, with or without a strong presence of Cu in the center column, and mainly observed at the precipitate-matrix interface. For alloy C, almost all precipitates showed multiple Cu-containing sub-units of β_{Cu}' in addition to Q'/C. For some precipitates, complete unit cells of Q' could be seen (e.g. Fig. 3g). The sub-units were not only observed at the precipitate-matrix interface, but also in the precipitate interior. Despite noted differences, β'' remained the dominant phase in both alloys at 12 h ageing.

At 24 h ageing (Fig. 3 i–l), the hybrid character had developed further in alloys S and C. Pure β'' phases were less common. For alloy S, the precipitates typically showed a predominantly Al-Mg-Si containing β'' phase and U2 phase interior, and some Cu enrichment, as well as a few sub-units of β_{Cu}' and Q'/C at the precipitate-matrix interface. For the precipitates exhibiting a high degree of fragmentation (e.g. Fig. 3i), unit cells of β'' were no longer present, but reduced to rows of- or individual β''-eyes. The observations are similar to other reports showing β''/fragmented precipitates at underaged and peak hardness conditions for alloys with higher Cu content [18, 43]. For alloy C, an increased proportion of the precipitate structures comprised Cu-containing phases, in particular Q'. Fig. 3k shows a pure Q' phase with characteristic lath-shaped morphology and coherent $\langle 150 \rangle_{Al}$ interfaces. This was not observed in alloy S at any ageing condition. Corresponding precipitates in alloy M at 24 h ageing (see Fig. 4 e–h) exhibited two

main precipitate types: hybrid rods (mainly S phase) and hybrid/fragmented laths with $\{100\}_{Al}$ habit planes (mainly L phase). Most precipitates showed significant Cu incorporation. Q′ phase and C phase unit cells were observed, as well as β_{Cu}' and Q′/C sub-units. β′ was also observed at this stage (Fig. 4h). Many precipitates in alloy M had developed an ordered Si-network permeating the precipitate structures. This further supports the indicated acceleration in transformation kinetics as compared to alloys S and C.

3.1.4. Significantly overaged precipitates (≥ 1 week ageing)

After 1 week ageing a large transformation of the precipitate structures in alloys S and C had taken place, and the precipitates had coarsened considerably (see Fig. 3m–p). For alloy S, the main phases observed were β′ and β_2'. These phases often dominated the interior of the precipitates. β′ and β_2' are closely related structures, differing primarily in the atomic modulation of the Si_1 column (see Fig. 2). The structure of proper β′ has 1 extra Si atom per 3×4.05 Å in the *c*-direction at the Si_1 columns, i.e. a $\frac{3}{4}a_{Al}$ repeat distance [45]. This leads to a higher column occupancy, and hence a higher intensity at the Si_1 site. β_2' shows absence of clear modulation, and is readily identified in a diffraction based approach due to a slight variation in space group symmetry [30]. In the following, β′ and β_2' are together denoted as $\beta_{(2)}'$. $\beta_{(2)}'$ was often linked by a row of U2 unit cells/sub-units to the Al matrix or phases at the precipitate-matrix interface. Q′/C sub-units and full unit cells of Q′ were commonly observed at the interface. In alloy C, the Q′ phase had now progressed to become the dominant phase observed. As shown in Fig. 3o, almost pure Q′ phases with characteristic $\langle 150 \rangle_{Al}$ interfaces were sometimes observed. In addition to Q′, $\beta_{(2)}'$ was also frequently seen. An ordered Si-network had been established in the precipitates of alloys S and C. The β_{Cu}' sub-unit was no longer observed in either alloy, which indicated that this sub-unit either dissolved or underwent a structural transition. No further ageing of alloy C was conducted, as the precipitates were thought to show limited subsequent change.

After 2 weeks ageing of alloy S, many precipitates showed modest coarsening relative to the 1 week condition, and the phases coexisting were similar to the 1 week state (see Fig. 3q, r). From the observation of a series of images, the main development seemed to be the increased extent of the Q′ phase, which now reached further into the precipitate interior. Multiple grouped Q′ unit cells were frequently observed.

At 1 month total ageing of alloy S there was limited further coarsening of the precipitates (see Fig. 3s, t). Similar to the 1 week–2 weeks transition, there seemed to be a further development of the Q′ takeover of the precipitate structures. In some precipitates there was now a near 50/50 division of $\beta_{(2)}'$ phase and Q′ phase. In addition to these phases, rows of U2 unit cells often formed the interfaces between the $\beta_{(2)}'$ and Q′ phases. The U2 phase was also often observed at the precipitate-matrix interface, particularly in the interlayer separating the $\beta_{(2)}'$ phase from the Al matrix. The interlayer forms because the $\beta_{(2)}'$ phase does not form coherent interfaces towards Al [41]. The Q′ phase however forms coherent interfaces along $\langle 150 \rangle_{Al}$ [42]. Several precipitates at 1 month ageing for alloy S showed many similarities with precipitates in alloy C at the 1 week condition. This further attested to the differences observed in phase transformation kinetics caused by the differences in the Cu content of these alloys.

Precipitates in alloy M after 1 month ageing showed significant differences as compared to alloy S after 1 month ageing, and compared to alloy C after 1 week ageing (see Fig. 4i–l). There were still two main precipitate types: hybrid rods (mainly S phase), which mainly comprised Q′ and $\beta_{(2)}'$, and laths with $\{100\}_{Al}$ habit planes. The lath-shaped precipitates were most frequent, are were predominantly L phase (see Fig. 5b), but C phase was also observed (see Fig. 4k). Atomic columns at the precipitate interfaces often showed clear Cu segregation. For the rod-shaped precipitates this often resulted in formation of rows of β_{Cu}' sub-units. For the lath-shaped precipitates this was manifested as C sub-units and C unit cells. The precipitates of alloy M had coarsened

substantially less than for alloys S and C in the overageing stages, which is likely due to the stabilising effect of the Cu enriched interfaces, which has been demonstrated for the C sub-unit on the interfaces of L phase precipitates [12, 46]. The β_{Cu}' sub-unit was not observed in the overaged precipitates in alloys S and C. In alloy M however, the β_{Cu}' sub-unit was commonly observed at the precipitate-matrix interface, also after 1 month total ageing. The β_{Cu}' sub-unit did not grow to form complete unit cells.

3.2. Quantification of the precipitate phase evolution based on SPED data

The lattice image results provide detailed insight to the complexity and interplay of the different phases in the Al-Mg-Si-Cu system. However, in order to provide stronger statistical support for the proposed evolution of precipitate phases inferred from lattice image observations, a recently developed SPED approach was applied [29, 30]. This approach enables determination of precipitate types for a large number of precipitates, obtained in large, representative areas of the alloy microstructures. Fig. 5 presents phase mapping results obtained from a SPED scan acquired in the microstructure of alloy M at the 1 month ageing condition. For the purpose of visualization, three groups of phases in this ageing condition are mapped using RGB colouring: Q′/C (red), L (green), and $\beta_{(2)}'$ (blue) (see Fig. 5b). The L phase (green) is seen to have a widespread presence, in agreement with lattice image observations. Some pixels appear mixed, e.g. as indicated by purple colouring. This corresponds to a mix of $\beta_{(2)}'$ (blue) and Q′/C (red). Such hybrid $\beta_{(2)}'$ and Q′ phase precipitates were also observed in lattice images (not shown).

Fig. 6 summarizes the main findings from the SPED experiments. These bar plots show the average precipitate phase fractions estimated in each ageing condition for alloys S, C, and M, encompassing a total of more than 5000 scanned precipitates. Additional SPED mapping results from which the plots in Fig. 6 are based are shown in **Figs. SI 8–10**. In accordance with TEM observations and established knowledge on the precipitation in the Al-Mg-Si(-Cu) system, Fig. 6 shows that the β″ phase dominates at the peak aged condition (3 h), and subsequently drops off with overageing. For alloys S and C, it is seen that the main transformation of phases occurred between the 24 h and the 1 week state. In this transition stage, the fraction of β″ is seen drop, and is replaced by an increased fraction of $\beta_{(2)}'$ phase and Q′ phase. At the 1 week ageing condition, the relative fraction Q′/$\beta_{(2)}'$ is shown to be much higher in alloy C as compared to alloy S, which agrees well with lattice image observations (see Fig. 3m–p). It is also seen that alloy S after 1 month ageing has a similar division of phases to that of alloy C after 1 week ageing. This is also in good agreement with the development inferred from lattice image observations.

SPED also showed that L type precipitates were present in alloys S and C. In alloy S, the L phase was often linked with microstructure defects such as dislocation lines [30]. This is in agreement with previous studies of this phase [12, 37, 38]. The same applies for alloy C, but here the phase mapping results indicated that a low number of L phases could also be observed away from microstructure heterogeneities.

Alloy M differs as expected notably from alloys S and C in the evolution of phases. At the 3 h condition, the microstructure is seen to comprise a lower fraction of β″ phase, and a higher fraction of L and $\beta_{(2)}'$ phases as compared to alloys S and C. A similar difference is observed at the 24 h condition, where the fraction of L and $\beta_{(2)}'$ phases has increased further for alloy M. The SPED analysis also shows that there is a widespread presence of the β″ phase at the 24 h condition. This result was not evident from HAADF-STEM imaging. At the 1 month condition, alloy M is dominated by the L phase. This evolution differs from that of alloys S and C, where it is $\beta_{(2)}'$ and Q′ that eventually dominate. SPED analysis results serve to demonstrate that there is a need for improvements in precipitate statistics in order to make general statements about the precipitation of age hardening Al alloys.
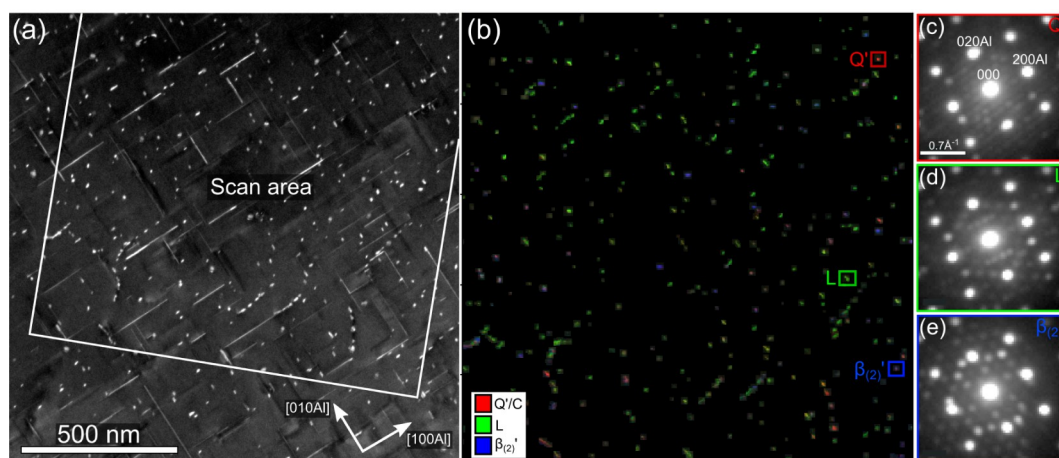
Fig. 5. (a) Dark-field TEM image of alloy M in the 1 month ageing condition. SPED scan area is indicated. The image was acquired near the $[001]_{Al}$ zone axis. (b) Phase map constructed from analysed SPED data showing 437 precipitate cross-sections. Three groups of phases are mapped using RGB colouring: Q′/C (red), L (green), and $\beta_{(2)}'$ (blue). (c–e) Individual pixel PED patterns (raw) from indicated precipitates in (b). (For interpretation of the references to colour in this figure legend, the reader is referred to the web version of this article.)

3.3. Connection between microstructure observations and bulk material phase transformations measured by DSC

In general, energy has to be supplied if chemical bonds are to dissociate, which refers to an endothermic reaction. In exothermic reactions, energy is released, which indicates that new chemical bonds have been formed. For Al alloys, dissolution of precipitate phases corresponds to an endothermic reaction, and precipitation belongs to exothermic reactions. The results from the DSC experiments conducted on alloys S and C are presented in Fig. 7. The main endo- and exothermic peaks are indicated in Roman numerals I–IX. The precipitation events are (coarsely) interpreted as follows: exothermic peak I — GP-zone and/or cluster formation; endothermic peak II — dissolution of GP-zones/clusters; exothermic peak III — β″ precipitation; endothermic peak IV — β″ dissolution; exothermic peak V — β′ (/and Q′) formation; endothermic peak VI — β′ (/and Q′) dissolution; exothermic peak VII — Q precipitation; exothermic peak VIII — β precipitation; endothermic peak IX — β (/and Q) dissolution.

It is important to emphasize that this is a simplified interpretation of the complex precipitation reactions previously elaborated through the study of precipitate structures. As shown, there were additional phases forming in these alloys, such as U2 and L phases. The vast majority of precipitates were also hybrid, each comprising multiple coexisting phases. It is here aimed at a qualitative understanding of the curves.

The curves from both alloys in all scanned ageing conditions nearly overlap up to the point of peak V. This indicates that all precipitation events up to this point were of similar character. The differences in the DSC curves occurred in the final stages of heating. It is seen that there are differences in the curves for alloys S and C between peaks V and IX for all ageing conditions. The differences observed between peaks V and VII are thought to arise due to variations in the formation and dissolution rate of hybrid Q′ phase and $\beta_{(2)}'$ phase precipitates. The HAADF-STEM and SPED experiments showed that these alloys formed different relative precipitate phase fractions of Q′/$\beta_{(2)}'$, seen from Fig. 3m–p and Fig. 6a, b. Differences in the relative fraction of Q′ phase to $\beta_{(2)}'$ phase implies differences in the kinetics of precipitate formation and dissolution, which are thought to have given rise to the variation observed.

The main differences between the DSC curves are observed at the subsequent formation and dissolution of equilibrium phases, i.e. cubic β phase and hexagonal Q phase. The formation/dissolution of pure diamond structure Si is thought to be approximately equal for alloys S and C due to the nearly equal levels of Si additions and the similar Si:Mg

ratio, and is therefore left out of the interpretation of the curves. Peak VII and peak VIII were interpreted as being due to the separate precipitation of the Q phase and the β phase, respectively. This interpretation again followed from the measurement of an increased relative precipitate phase fraction Q′/$\beta_{(2)}'$ in alloy C as compared to alloy S at the 1 week isothermal ageing condition (see Fig. 6a, b). Furthermore, the precipitates in alloy C were sometimes observed to hold defining pure Q′ phase characteristics, such as coherent $\langle 150 \rangle_{Al}$ precipitate-matrix interfaces (see Fig. 3o). The precipitates of alloy C exhibiting the highest relative precipitate phase fraction Q′/$\beta_{(2)}'$ and defining interfaces are thought to be the precipitates that have subsequently transformed to equilibrium Q phase. For alloy S, peak VII is apparently missing, which means that this alloy does not form Q phase. This indicated that the predominantly $\beta_{(2)}'$ precipitates of this alloy (see Fig. 3m, n and Fig. 6a) transformed as pure β′ phase precipitates, i.e. having formed equilibrium β in the final precipitation stage.

For alloy C, the heat signals of peak VII and peak VIII have some overlap, causing the exothermic effect of Q precipitation to appear as a local minimum on a larger exothermic β precipitation peak. The integrated peak area of peak VIII (β) is much larger than peak VII (Q), implying that also for alloy C the main equilibrium phase is β. This was expected considering the low total Cu addition. Peak VIII is also shifted to a higher temperature in the case of alloy C, indicating that the formation of β has a higher energy barrier in this alloy. Peak VII (Q phase formation) could also potentially be missing from the DSC curve of alloy S due to complete overlap with peak VIII (β phase formation), i.e. that there is an insufficient amount of heat released for the Q phase formation to be detected. This difference in equilibrium phase precipitation is an interesting finding, which shows support for a suggestion made by Bobel et al. [11], who suggested that the presence of small Cu additions determine the stability of hexagonal Q phase or cubic β phase upon ageing to equilibrium conditions.

3.4. Evaluation of the formation of Cu-containing sub-units

β″ was the dominant phase in all alloys studied at the peak hardened condition (3 h), as seen from Fig. 6. Therefore, in order to understand the subsequent evolution of the precipitate crystal structures at the atomic level, it is reasonable to start by inspecting how Cu enters and affects the crystal structure of the β″ phase (see Fig. 8). There are six distinct atomic positions in the β″ structure: Mg_1, Mg_2, Mg_3, Si_1, Si_2, and $Al/(/Si_3)$ (see Fig. 2). Density functional theory (DFT) calculations have shown that Cu atoms have highest affinity for the $Al(/Si_3)$
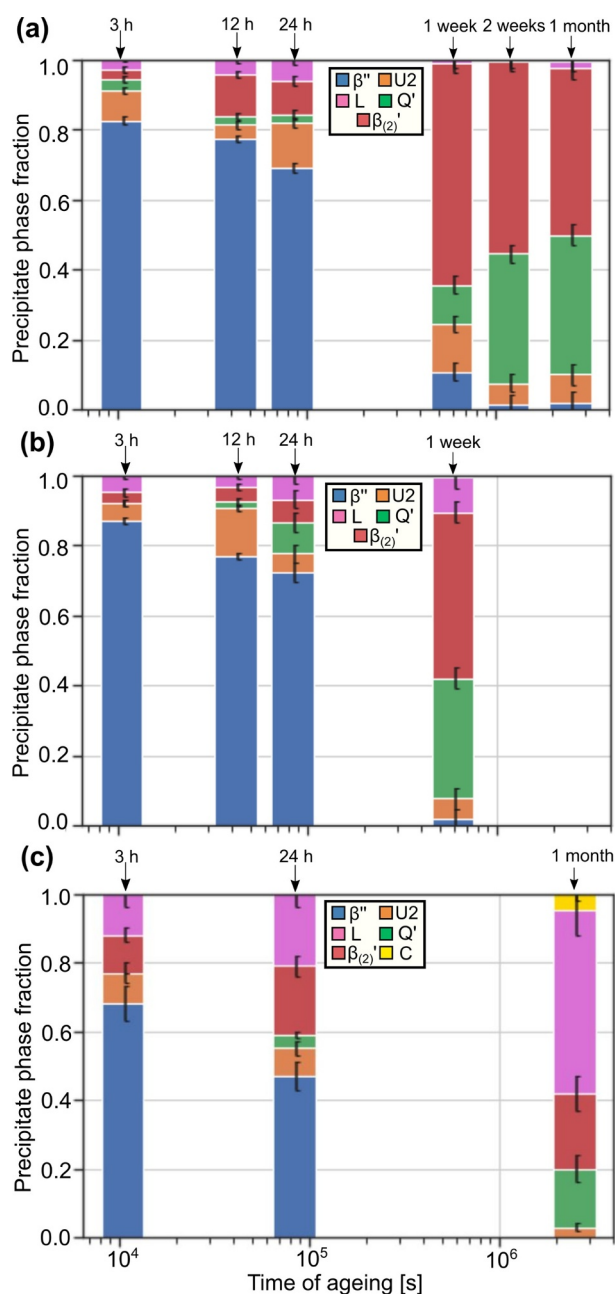
Fig. 6. Bar plots showing average precipitate phase fractions in alloy (a) S, (b) C, and (c) M in each indicated ageing condition. The numbers are estimated from SPED data.

positions, a moderate affinity for the Si_1 position, and to some extent also the Si_2 position [39]. The Mg positions were shown not to be favoured.

Cu has not previously been demonstrated to show clear occupation of the Si_1 and Si_2 positions in the β'' structure. However, the similarities in the structures of the β''-eye and the GPB-zones in the Al-Mg-Cu system [47], in addition to some support from DFT calculations, indicate that these might be potential points of entry for Cu atoms. The Si_1 and Si_2 columns are situated on the Si-network. These columns are also in proximity of both Al and Mg columns which is also part of the β_{Cu}' sub-unit. Therefore, a gradual replacement of either the Si_1 or Si_2 column by Cu may be the probable starting point of the β_{Cu}' sub-unit. Fig. 8a–d shows lattice images and atomic overlays of a pure β'' precipitate and a precipitate containing β'' phase and β_{Cu}' sub-units. On comparison of the images in Fig. 8a, b and in Fig. 8c, d, it is seen that the Cu column of β_{Cu}'

is positioned in close proximity of the Si_1 and Si_2 positions of the pure β'' structure. The triangular β_{Cu}' site is observed to interrupt the ordering of the β''-eyes. The net effect of this structural change is inclusion of Cu, and the establishment of an increasingly ordered Si-network, which is favoured on the basis of lattice image observations. Hence, in contrast to the GPB-zones of the Al-Mg-Cu system, the structure of β''-eyes in the Al-Mg-Si-Cu system seems to be immediately perturbed by the inclusion of Cu, which forms β_{Cu}' sub-units near the Si_1 and Si_2 positions. Another interesting remark is that although the interfaces towards the Al matrix are identical for the structures in Fig. 8c and d, there is a shift in the heights of the corresponding atomic positions in the remainder of the precipitate structures that are not in the immediate neighbourhood of the β_{Cu}' sub-units. In fact, all atomic positions in the left-hand row of three β''-eyes in Fig. 8c are shifted $1/2a_{Al}$ in height relative to the corresponding row of three β''-eyes in Fig. 8d. This indicates that there are additional, non-site specific structural changes occurring in the transformation towards post β''-phases, which in this case may have been triggered by the Cu inclusions.

Previous TEM reports have shown that Cu mainly enriches the Al ($/Si_3$) columns of the β'' structure [48, 49], which as noted was also favoured from DFT-based calculations. Observations of multiple β'' lattice images show that this is also supported from this work. Fig. 8e–h shows lattice images of a pure β'' precipitate and a precipitate containing β''-eyes and a Q' unit cell. On comparison of the images in Fig. 8e, f and in Fig. 8g, h, it is seen how the β'' structure connects to the Q' unit cell. The positioning of the Cu column corresponds well with the Al($/Si_3$) site of the β'' structure. As the Al($/Si_3$) column is positioned in-between the Si-network, enrichment of this column leads to a Cu-containing column characteristic of the Q' (and C) phase. This shows that Cu enrichment of the Al($/Si_3$) column is one possible starting point for the formation of Q'/C sub-units.

The C sub-unit only existed at the precipitate-matrix interface (see Fig. 4), and therefore differs notably from the β_{Cu}' and the Q'/C sub-units. Hence, the C sub-unit does not form as the result of Cu inclusions in a structure such as β'', but rather due to an interaction with the atoms positioned at the precipitate-matrix interface. The Cu column of this sub-unit is not embedded in- or replacing the Si-network columns, but rather positioned externally to it (see **Fig. SI 7**). The C sub-unit was frequently observed in alloy M, and only very rarely in alloy C. It therefore seems that an increased Mg:Si ratio is necessary in order to form this sub-unit. The C sub-unit was observed in a Mg-rich (Mg:Si ≈ 2:1) alloy containing only 0.01 wt.% Cu [40]. It is therefore the high Si:Mg ratio, and not the total Cu content that is preventing alloys S and C from forming notable numbers of C sub-units.

4. Conclusions

A combination of HAADF-STEM lattice imaging, SPED-based phase quantification, and DSC has been applied to study the effect of low Cu additions on the evolution of precipitate crystal structures in three Al-Mg-Si(-Cu) alloys during overageing. Generally, the precipitates in all alloys studied showed a gradually increasing proportion of Cu-containing phases with overageing, and accelerated phase transformation kinetics were observed with higher Cu content.

Three different Cu-containing sub-units were identified as the building blocks for all Al-Mg-Si-Cu phases. They are
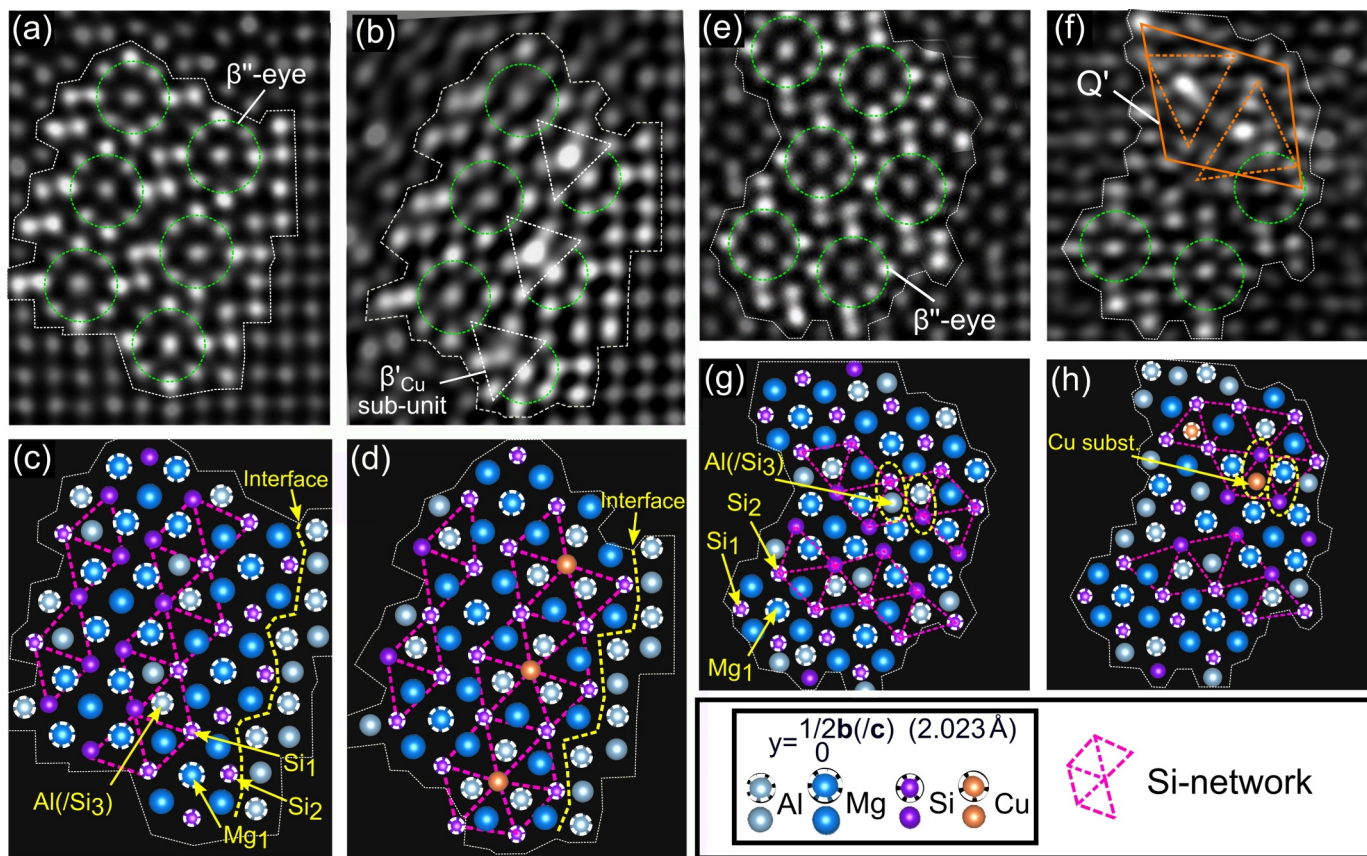
- β_{Cu}' sub-units
- Q'/C sub-units
- C sub-units

The origins of the two first sub-units were discussed based on how Cu inclusions would alter the β'' crystal structure. The latter only forms at the precipitate-matrix interface, and primarily in Mg-rich alloys.

Two Si-rich alloys and one Mg-rich alloy were studied, and the main findings can be summarised as
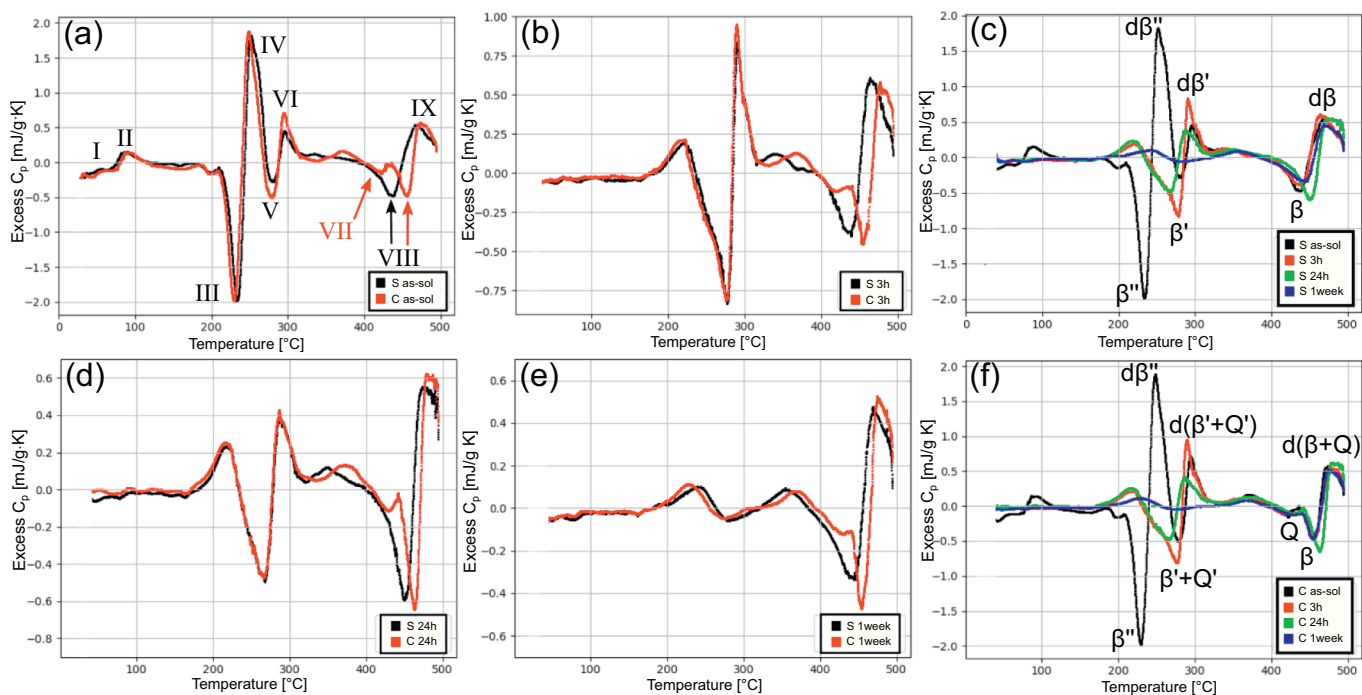
Fig. 7. Excess specific heat capacity measured as a function of temperature obtained from experimental DSC curves for alloys S and C in the ageing conditions: (a) as-solutionized (as-sol) (b) 3 h (d) 24 h (e) 1 week. (c) Combined measurements for alloy S and (f) combined measurements for alloy C. The main endo- and exothermic peaks (I–IX) are indicated. A and dA denote formation and dissolution of a given phase A, respectively.

Fig. 8. (a–d) Side-by-side lattice images and atomic overlays of a pure β″ and a hybrid precipitate containing β″ and β$_{Cu}$′ sub-units. (e–h) Side-by-side lattice images and atomic overlays of a pure β″ and a hybrid precipitate containing β″-eyes and a Q′ unit cell. Atomic overlay of the lattice images have been constructed according to the rules of Andersen et al. [17].

- Hybrid $\beta_{(2)}'$ phase and Q′ phase precipitates were formed upon overageing in the Si-rich alloys, and the evolution involved a gradually increasing phase fraction of the Cu-containing Q′ phase
- Minor changes to the Cu level in the Si-rich alloys determined the stability of hexagonal Q phase relative to cubic β phase
- L phase precipitates existed in all conditions in the Mg-rich alloy, and exhibited significantly improved thermal stability as compared to the hybrid $\beta_{(2)}'$ phase and Q′ phase precipitates in the Si-rich alloys

Our study demonstrates how relatively small changes in alloy compositions can cause significant changes to the precipitation. The differences in precipitation were inferred from the analysis of 1000s of precipitate phases enabled by the SPED approach. The improved statistics and the increased objectivity this approach offers validate it as a powerful tool that will be of importance in future alloy design.

Declaration of competing interest

The authors declare that they have no known competing financial interests or personal relationships that could have appeared to influence the work reported in this paper.

Acknowledgments

Appendix A. Supplementary Information

The **Supplementary Information** following this publication presents additional HAADF-STEM lattice images, conventions regarding classification of Al-Mg-Si(-Cu) phases, an atomic overlay of a precipitate lattice image, as well as additional SPED phase mapping results from selected ageing conditions in the studied alloys. The **Supplementary Information** is available to download from [https://doi.org/10.1016/j.matchar.2019.110087]. The raw SPED data required to reproduce these findings cannot be shared at this time due to technical limitations, but are available upon reasonable request.

References

[1] G.E. Totten, D.S. MacKenzie, Handbook of Aluminum, vol. I and II, Marcel Dekker, New York, 2003.

[2] W.S. Miller, L. Zhuang, J. Bottema, A.J. Wittebrood, P. De Smet, A. Haszler, A. Vieregge, Recent development in aluminium alloys for the automotive industry, Mater. Sci. Eng. A 280 (2000) 37–49.

[3] M. Murayama, K. Hono, Pre-precipitate clusters and precipitation processes in Al-Mg-Si alloys, Acta Mater. 47 (1999) 1537–1548.

[4] A.K. Gupta, D.J. Lloyd, S.A. Court, Precipitation hardening in Al-Mg-Si alloys with and without excess Si, Mater. Sci. Eng. A 316 (2001) 11–17.

[5] G.A. Edwards, K. Stiller, G.L. Dunlop, M.J. Couper, The precipitation sequence in Al-Mg-Si alloys, Acta Mater. 46 (1998) 3893–3904.

[6] C.D. Marioara, S.J. Andersen, H.W. Zandbergen, R. Holmestad, The influence of alloy composition on precipitates of the Al-Mg-Si system, Metall. Mater. Trans. A 36 (2005) 691–702.

[7] W.F. Miao, D.E. Laughlin, Effects of Cu content and preageing on precipitation characteristics in aluminium alloy 6022, Metall. Mater. Trans. A 31 (2000) 361–371.

[8] M. Murayama, K. Hono, W.F. Miao, D.E. Laughlin, The effect of Cu additions on the precipitation kinetics in an Al-Mg-Si alloy with excess Si, Metall Mater. Trans. A 32

(2001) 239–246.

[9] Z. Jia, L. Ding, L. Cao, R. Sanders, S. Li, Q. Liu, The influence of composition on the clustering and precipitation behavior of Al-Mg-Si-Cu alloys, Metall. Mater. Trans. A 48 (2014) 459–473.

[10] M.W. Zandbergen, A. Cerezo, G.D.W. Smith, Study of precipitation in Al–Mg–Si alloys by atom probe tomography II. Influence of Cu additions, Acta Mater. 101 (2015) 149–158.

[11] A. Bobel, K. Kim, C. Wolverton, M. Walker, G.B. Olson, Equilibrium composition variation of Q-phase precipitates in aluminum alloys, Acta Mater. 138 (2017) 150–160.

[12] C.D. Marioara, S.J. Andersen, J. Røyset, O. Reiso, S. Gulbrandsen-Dahl, T.-E. Nicolaisen, I.-E. Opheim, J.F. Helgaker, R. Holmestad, Improving thermal stability in Cu-containing Al-Mg-Si alloys by precipitate optimization, Metall. Mater. Trans. A 45 (2014) 2938–2949.

[13] C. Cayron, L. Sagalowicz, O. Beffort, P.A. Buffat, Structural phase transition in Al-Cu-Mg-Si alloys by transmission electron microscopy study on an Al-4 wt% Cu-1 wt% Mg-Ag alloy reinforced by SiC particles, Philos. Mag. 79 (1999) 2833–2851.

[14] K. Matsuda, Y. Uetani, T. Sato, S. Ikeno, Metastable phases in an Al-Mg-Si alloy containing copper, Metall. Mater. Trans. A 32 (2001) 1293–1299.

[15] D.J. Chakrabarti, D.E. Laughlin, Phase relations and precipitation in Al–Mg–Si alloys with Cu additions, Prog. Mater. Sci. 49 (2004) 389–410.

[16] C.D. Marioara, S.J. Andersen, T.N. Stene, H. Hasting, J. Walmsley, A.T.J. van Helvoort, R. Holmestad, The effect of Cu on precipitation in Al-Mg-Si alloys, Philos. Mag. 87 (2007) 3385–3413.

[17] S.J. Andersen, C.D. Marioara, J. Friis, R. Bjørge, Q. Du, I.G. Ringdalen, S. Wenner, E.A. Mørtsell, R. Holmestad, T. Saito, J. Røyset, O. Reiso, Directionality and column arrangement principles of precipitates in Al-Mg-Si(-Cu) and Al-Mg-Cu linked to line defect in Al, Mater. Sci. Forum 877 (2017) 461–470.

[18] T. Saito, C.D. Marioara, S.J. Andersen, W. Lefebvre, R. Holmestad, Aberration-corrected HAADF-STEM investigations of precipitate structures in Al-Mg-Si alloys with low Cu additions, Philos. Mag. 94 (2014) 520–531.

[19] T. Saito, E.A. Mørtsell, S. Wenner, C.D. Marioara, S.J. Andersen, J. Friis, K. Matsuda, R. Holmestad, Atomic structures of precipitates in Al-Mg-Si alloys with small additions of other elements, Adv. Eng. Mater. 20 (2018) 1800125.

[20] S.J. Andersen, C.D. Marioara, J. Friis, S. Wenner, R. Holmestad, Precipitates in aluminium alloys, Adv. Phys. X 3 (2018) 790–813.

[21] W.J. Liang, P.A. Rometsch, L.F. Cao, N. Birbilis, General aspects related to the corrosion of 6xxx series aluminium alloys: exploring the influence of Mg/Si ratio and Cu, Corros. Sci. 76 (2013) 119–128.

[22] G. Svenningsen, M.H. Larsen, J.C. Walmsley, J.H. Nordlien, K. Nisancioglu, Effect of artificial aging on intergranular corrosion of extruded AlMgSi alloy with small Cu content, Corros. Sci. 48 (2006) 1528–1543.

[23] S.K. Kairy, P.A. Rometsch, K. Diao, J.F. Nie, C.H.J. Davies, N. Birbilis, Exploring the electrochemistry of 6xxx series aluminium alloys as a function of Si to Mg ratio, Cu content, ageing conditions and microstructure, Electrochim. Acta 190 (2016) 92–103.

[24] M.H. Larsen, J.C. Walmsley, O. Lunder, R.H. Mathiesen, K. Nisancioglu, Intergranular corrosion of copper-containing AA6xxx AlMgSi aluminum alloys, J. Electrochem. Soc. 155 (2008) 550–556.

[25] S.K. Kairy, T. Alam, P.A. Rometsch, C.H.J. Davies, R. Banerjee, N. Birbilis, Understanding the origins of intergranular corrosion in copper-containing Al-Mg-Si alloys, Metall. Mater. Trans. A 47 (2016) 985–989.

[26] C.D. Marioara, A. Lervik, J. Grønvold, O. Lunder, S. Wenner, T. Furu, R. Holmestad, The correlation between intergranular corrosion resistance and copper content in the precipitate microstructure in an AA6005a alloy, Metall Mater Trans A 49 (2018) 5146–5156.

[27] T. Saito, S. Muraishi, C.D. Marioara, S.J. Andersen, J. Røyset, R. Holmestad, The effects of low cu additions and predeformation on the precipitation in a 6060 Al-Mg-Si alloy, Metall. Mater. Trans. A 44 (2013) 4124–4135.

[28] J.A.S. Green, Aluminum Recycling and Processing for Energy Conservation and Sustainability, 91 ASM International, Materials Park, OH, 2007, pp. 109–134.

[29] J.K. Sunde, Ø. Paulsen, S. Wenner, R. Holmestad, Precipitate statistics in an Al-Mg-Si-Cu alloy from scanning precession electron diffraction data, J. Phys.: Conf. Ser. 902 (2017) 12022.

[30] J.K. Sunde, C.D. Marioara, A.T.J. van Helvoort, R. Holmestad, The evolution of precipitate crystal structures in an Al-Mg-Si(-Cu) alloy studied by a combined HAADF-STEM and SPED approach, Mater. Charact. 142 (2018) 458–469.

[31] P. Moeck, S. Rouvimov, E.F. Rauch, M. Véron, H. Kirmse, I. Häusler, W. Neumann, D. Bultreys, Y. Maniette, S. Nicolopoulos, High spatial resolution semi-automatic crystallite orientation and phase mapping of nanocrystals in transmission electron microscopes, Cryst. Res. Technol. 46 (2011) 589–606.

[32] J.S. Barnard, D.N. Johnstone, P.A. Midgley, High-resolution scanning precession electron diffraction: alignment and spatial resolution, Ultramicroscopy 174 (2017) 79–88.

[33] F. de la Peña, et al., HyperSpy - 1.5.2, (2019), https://doi.org/10.5281/zenodo.3396791.

[34] S.M. Sarge, G.W.H. Höhne, W.F. Hemminger, Calorimetry: Fundamentals, Instrumentation and Applications, Wiley-VCH Verlag GmbH & Co. KGaA, Weinheim, Germany, 2014.

[35] P.D. Nellist, S.J. Pennycook, The principles and interpretation of annular dark–field Z–contrast imaging, Adv. Imag. Electron Phys. 113 (2000) 148–203.

[36] C.D. Marioara, J. Nakamura, K. Matsuda, S.J. Andersen, R. Holmestad, T. Sato, T. Kawabata, S. Ikeno, HAADF-STEM study of β′-type precipitates in an over-aged Al-Mg-Si-Ag alloy, Philos. Mag. 92 (2012) 1149–1158.

[37] M. Torsæter, F.J.H. Ehlers, C.D. Marioara, S.J. Andersen, R. Holmestad, Applying precipitate–host lattice coherency for compositional determination of precipitates

in Al-Mg-Si-Cu alloys, Philos. Mag. (2012) 3833–3856.

[38] M. Torsæter, W. Lefebvre, C.D. Marioara, S.J. Andersen, J.C. Walmsley, R. Holmestad, Study of intergrown L and Q′ precipitates in Al-Mg-Si-Cu alloys, Scripta Mater. 64 (2011) 817–820.

[39] T. Saito, F.J.H. Ehlers, W. Lefebvre, D. Hernandez-Maldonado, R. Bjørge, C.D. Marioara, S.J. Andersen, E.A. Mørtsell, R. Holmestad, Cu atoms suppress misfit dislocations at the β″/Al interface in Al-Mg-Si alloys, Scr. Mater. 110 (2016) 6–9.

[40] Y. Weng, Z. Jia, L. Ding, K. Du, H. Duan, Q. Liu, X. Wu, Special segregation of Cu on the habit plane of lath-like β′ and QP2 precipitates in Al-Mg-Si-Cu alloys, Scripta Mater. 151 (2018) 33–37.

[41] K. Teichmann, C.D. Marioara, S.J. Andersen, K. Marthinsen, TEM study of β′ precipitate interaction mechanisms with dislocations and β′ interfaces with the aluminium matrix in Al-Mg-Si alloys, Mater. Charact. 75 (2013) 1–7.

[42] C.D. Marioara, J. Friis, E. Hersent, A. Oskarsson, A transmission electron microscopy study of precipitate phases that form during operation in a heat exchanger alloy, Mater. Charact. 149 (2019) 218–225.

[43] L. Ding, Z. Jia, J.F. Nie, Y. Weng, L. Cao, H. Chen, X. Wu, Q. Liu, The structural and compositional evolution of precipitates in Al-Mg-Si-Cu alloy, Acta Mater. 145 (2018) 437–450.

[44] T. Maeda, K. Kaneko, T. Namba, Y. Koshino, Y. Sato, R. Teranishi, Y. Aruga, Structural and compositional study of precipitates in under-aged Cu-added Al-Mg-Si alloy, Sci. Rep. 8 (2018) 16629.

[45] R. Vissers, M.A. van Huis, J. Jansen, H.W. Zandbergen, C.D. Marioara, S.J. Andersen, The crystal structure of the β′ phase in Al-Mg-Si alloys, Acta Mater. 55 (2007) 3815–3823.

[46] J.K. Sunde, S. Wenner, R. Holmestad, In situ heating TEM observations of evolving nanoscale Al-Mg-Si-Cu precipitates, J. Microsc. (2019), https://doi.org/10.1111/jmi.12845.

[47] L. Kovarik, S.A. Court, H.L. Fraser, M.J. Mills, GPB zones and composite GPB/GPBII zones in Al-Cu-Mg alloys, Acta Mater. 56 (2008) 4804–4815.

[48] S. Wenner, L. Jones, C.D. Marioara, R. Holmestad, Atomic-resolution chemical mapping of ordered precipitates in Al alloys using energy-dispersive X-ray spectroscopy, Micron 96 (2017) 103–111.

[49] K. Li, A. Béché, M. Song, G. Sha, X. Lu, K. Zhang, Y. Du, S.P. Ringer, D. Schryvers, Atomistic structure of Cu-containing β″ precipitates in an Al-Mg-Si-Cu alloy, Scr. Mater. 75 (2014) 86–89.